

# Simulating excitation spectra with projected entangled-pair states

Laurens Vanderstraeten,<sup>1,\*</sup> Jutho Haegeman,<sup>1</sup> and Frank Verstraete<sup>1,2</sup>

<sup>1</sup>*Department of Physics and Astronomy, University of Ghent, Krijgslaan 281, 9000 Gent, Belgium*

<sup>2</sup>*Vienna Center for Quantum Science and Technology, Faculty of Physics, University of Vienna, Boltzmannngasse 5, 1090 Vienna, Austria*

We develop and benchmark a technique for simulating excitation spectra of generic two-dimensional quantum lattice systems using the framework of projected entangled-pair states (PEPS). The technique relies on a variational ansatz for capturing quasiparticle excitations on top of a PEPS ground state. Our method perfectly captures the quasiparticle dispersion relation of the square-lattice transverse-field Ising model, and reproduces the spin-wave velocity and the spin-wave anomaly in the square-lattice Heisenberg model with high precision.

Quantum phases of matter are commonly characterized by the order of the ground states that are realized in many-body systems at zero temperature. Yet, the most interesting manifestations, both from the theoretical and the experimental perspective, of a given quantum phase are more related to the low-energy excitations on top of the ground state. In the case of strongly-correlated quantum phases these excitations typically have a collective nature, in the sense that they cannot be adiabatically connected to the excitations of a free system. Therefore, perturbative expansions or mean-field approximations do not allow for an accurate description, and more advanced conceptual and numerical tools have to be devised to understand their properties. This is especially true for one- and two-dimensional quantum systems, where strong quantum correlations often lead to collective excitations with fractionalized quantum numbers and anyonic statistics.

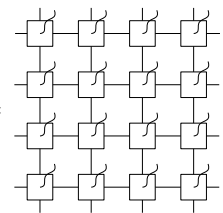
Tensor networks have emerged as a natural language for describing quantum phases of matter. It has been realized that these phases are characterized by the entanglement structure of their low-energy states, and that this structure can be captured by the class of tensor-network states<sup>1,2</sup>. In one dimension, this yields the well-known class of matrix product states<sup>3</sup> (MPS) describing ground states of generic spin chains, as well as a powerful formalism for capturing quasiparticle excitations on top of these strongly-correlated background states<sup>4</sup>. In this formalism, elementary excitations of the fully-interacting quantum Hamiltonian<sup>5</sup> are naturally interpreted as interacting particles (including magnons, triplons spinons, chargeons, holons, etc.<sup>6</sup>) and a two-particle S matrix can be defined and computed<sup>7</sup>. For two-dimensional systems, the class of projected entangled-pair states (PEPS)<sup>8</sup> provides the correct parametrization of ground states, and PEPS constructions for describing quasiparticles such as spinons<sup>9</sup> and anyons<sup>10,11</sup> have been proposed.

Yet, these constructions of quasiparticles against a PEPS background have been used numerically on fine-tuned wavefunctions only<sup>12,13</sup>, and have

not been applied variationally to characterize the spectrum of a given model Hamiltonian. Indeed, PEPS simulations have been restricted to the study of ground-state properties of ordered quantum magnets<sup>14–17</sup>, (chiral) spin liquids<sup>18–20</sup>, and strongly-correlated electrons<sup>16,21</sup>, but, thanks to considerable progress in MPS techniques<sup>22,23</sup>, in recent years a second generation of PEPS algorithms has started to form. The variational optimization of PEPS ground-state approximations has been made possible<sup>24,25</sup>, which allows to obtain higher accuracy on ground-state energies and order parameters. This, in turn, has made it possible to develop accurate extrapolation techniques<sup>26,27</sup>. In addition, quantities such as momentum-resolved structure factors or the energy variance can be computed with high accuracy<sup>25</sup>.

These techniques now make it possible to go beyond ground-state properties, and to simulate the excitation spectrum of a given Hamiltonian with PEPS. A first step was taken in Ref. 22, but limited to the special case of frustration-free Hamiltonians. In this work, we generalize this framework to simulate the excitation spectrum of generic Hamiltonians on two-dimensional lattices in the thermodynamic limit directly, and benchmark this method on the transverse-field Ising model and the square-lattice Heisenberg model.

*The algorithm*— The PEPS simulation of the excitation spectrum of a given model Hamiltonian  $H = \sum_i h_i$  consists of two steps. In a first step, we find an optimal approximation for the model's ground state in terms of a PEPS tensor  $A$ . The ground-state wavefunction can be written down as

$$|\Psi(A)\rangle = \text{contraction of a 4x4 grid of } A \text{ tensors}, \quad (1)$$


which represents the contraction of an infinite net-



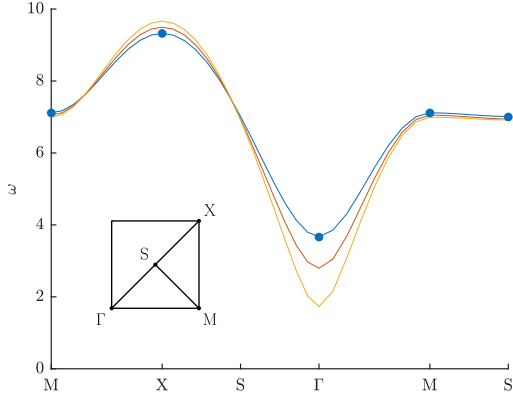


FIG. 1. The quasiparticle dispersion for the square-lattice transverse-field Ising model at  $\lambda = 2.5$  (blue),  $\lambda = 2.7$  (red) and  $\lambda = 2.9$  (yellow), as computed from PEPS with bond dimension  $D = 3$  and environment bond dimension  $\chi = 50$ . The blue dots are series-expansion data points extracted from Ref. 30.

a number of one-dimensional contractions. We refer to the supplemental material for a full exposition of all tensor-network diagrams. The hardest diagrams, and therefore the computational complexity of implementing the generalized eigenvalue problem [Eq. (6)], scales as  $\mathcal{O}(D^6\chi^3 + D^8\chi^2)$ .

*Benchmark results*—As a first example we test our method on the transverse-field Ising model, defined by the Hamiltonian

$$H_{\text{ising}} = - \sum_{\langle ij \rangle} S_i^z S_j^z + \lambda \sum_i S_i^x. \quad (8)$$

This model exhibits a quantum phase transition at  $\lambda_c \approx 3.044$  from a symmetry-broken phase ( $\lambda < \lambda_c$ ) to a polarized phase ( $\lambda > \lambda_c$ ). In Ref. 25 it was shown that the ground state of this model can be accurately approximated as a PEPS across the phase transition.

We can now build excitations on top of this ground state, and compute the quasiparticle spectrum. In Fig. 1 our results are plotted for the quasiparticle dispersion relation at three different values of the field; for one value of the field we compare with results from series expansions<sup>30</sup>. The dispersion clearly reaches a minimum at momentum  $\vec{q} = (0, 0)$ , yielding the value of the gap. The phase transition is signalled by the vanishing of the excitation gap; in fact, close to the phase transition, the gap should obey a scaling relation with a critical exponent  $\nu \approx 0.6230$ <sup>30</sup>. In Fig. 2 we have plotted the gap as a function of the field, showing that the power-law scaling is reproduced over a large region. We find estimates for the critical exponent  $\nu$  and the critical field  $\lambda$  within a percent precision.

A more challenging and interesting benchmark

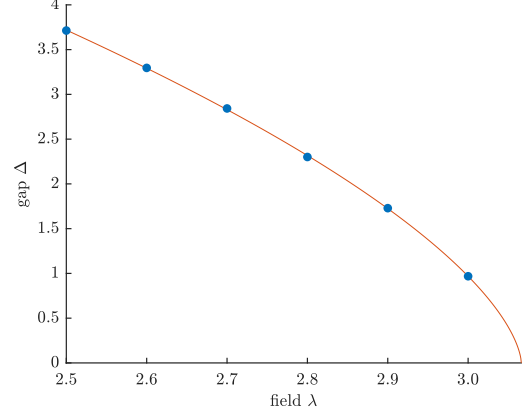


FIG. 2. The gap of the Ising model as a function of the field  $\lambda$ , with a fit  $\Delta \propto |\lambda - \lambda_c|^\nu$ ; we find  $\lambda_c \approx 3.066$  and  $\nu \approx 0.627$ . We have used  $D = 3$  and  $\chi = 50$ .

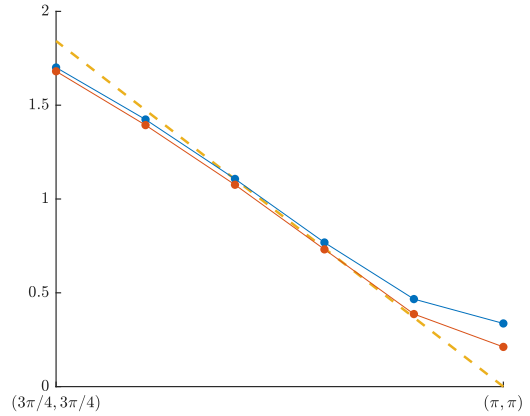


FIG. 3. The dispersion relation of the Heisenberg model approaching the gapless point  $(\pi, 0)$  with bond dimension  $D = 3$  (blue) and  $D = 4$  (red) and environment bond dimension up to  $\chi = 100$ , as compared to the linear dispersion relation with  $v_s \approx 1.65847$ <sup>31</sup> (yellow). Clearly, the finite bond dimension of the PEPS induces an artificial gap, which grows smaller as  $D$  increases. If we estimate the spin-wave velocity as the slope at the inflection point in the  $D = 4$  curve, we find  $v_s \approx 1.638$ .

is provided by the Heisenberg model, defined by the Hamiltonian

$$H_{\text{heis}} = \sum_{\langle ij \rangle} S_i^x S_j^x - S_i^y S_j^y - S_i^z S_j^z. \quad (9)$$

Here we have introduced the minus signs through a sublattice rotation of the original Heisenberg Hamiltonian, such that the staggered magnetization is mapped to a uniform one. Therefore, we can approximate the ground state as a uniform PEPS with a one-site unit cell<sup>25</sup>.

Since the ground state breaks a continuous symmetry, the spectrum exhibits a gapless Goldstone mode. The slope of the dispersion relation around

	$(\pi/2, \pi/2)$	$(\pi, 0)$
QMC <sup>34</sup>	2.4085	2.13
pCUT <sup>35</sup>	2.375	2.2
ED <sup>36</sup>	2.4144	2.2281
DMRG	2.40	2.06-2.07
$D = 4$	2.39	2.19

TABLE I. The estimates for the excitation energies at wavevectors  $\vec{q} = (\pi/2, \pi/2)$  and  $\vec{q} = (\pi, 0)$  as computed by some state-of-the-art numerical techniques, and compared to our PEPS result at  $D = 4$ .

the gapless point or spin-wave velocity  $v_s$  is a crucial quantity in any low-energy field theory for this model<sup>32,33</sup> and is directly accessible in e.g. neutron-scattering experiments. In Fig. 3 we have plotted the dispersion relation in a small portion of the Brillouin zone where the gap is expected to close. Because the finite bond dimension induces a finite correlation length in the ground state<sup>26,27</sup>, the dispersion relation exhibits an artificial gap. This effect is clearly seen in our results, but is diminished as the bond dimension increases. Besides this effect, we reproduce the linear dispersion and we obtain an estimate for the spin-wave velocity that is close to the Monte-Carlo estimate.

A more interesting feature of the spectrum is the shape of the dispersion relation at higher energies. Linear spin-wave theory predicts that the excitation gap is constant on the line between the wavevectors  $(\pi, 0)$  and  $(\pi/2, \pi/2)$ , but various numerical approaches<sup>34–40</sup> and experimental measurements<sup>41</sup> have shown that the excitation energy is suppressed at  $(\pi, 0)$  and elevated at  $(\pi/2, \pi/2)$  as compared to the spin-wave result. The physical origin of this discrepancy has been argued to follow from spinon deconfinement around the wavevector  $(\pi, 0)$ . In Fig. 4 we have plotted our results for the dispersion in this region, showing a significant dip in the dispersion. In Table I we compare our excitation energies to some other numerical results available in the literature. As to the physical origin of the spin-wave anomaly, we should note that the fact that our quasiparticle ansatz can accurately reproduce the excitation energy at  $(\pi, 0)$  suggests that this state is quite far from a deconfined two-spinon state.

*Outlook*— In this work we have presented a PEPS method for simulating excitation spectra of generic Hamiltonians in two dimensions, and have benchmarked the method on the Ising and Heisenberg models on the square lattice. The method can be readily extended to other lattice structures and PEPS ground states with larger unit cells. Although we have applied it to models that exhibit a local order parameter, our method can be ap-

plied equally well to more exotic quantum phases

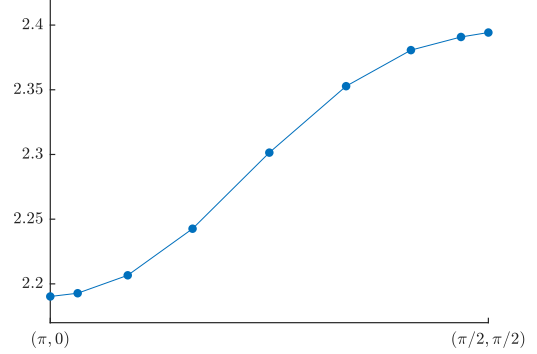


FIG. 4. The dispersion relation of the Heisenberg model between the points  $(\pi, 0)$  and  $(\pi/2, \pi/2)$ , computed with PEPS at  $D = 4$  and  $\chi = 100$ .

such as spin liquids and systems with topological order. In particular, the PEPS framework allows to directly target the fractionalized quasiparticles in these systems.

On the technical side many improvements of the method can be made. The conditioning of the generalized eigenvalue problem is, due to small eigenvalues in the effective norm matrix  $\mathbf{N}_{\vec{q}}$ , a source of large errors, and, therefore, a well-chosen preconditioner is required. Also, the implementation of  $\mathbf{H}_{\vec{q}}$  requires the contraction of a large number of different diagrams and is therefore computationally demanding; better contraction schemes can speed up the simulations considerably. This, in turn, would make higher values of the PEPS bond dimension feasible, which would enable the use of extrapolation techniques for e.g. the excitation energies. Finally, the exploitation of symmetries in the PEPS representation of the ground state as well as the quasiparticle excitations will lead to much more efficient simulations.

In the context of matrix product states, this method of describing excitation spectra falls within the set of so-called tangent-space methods<sup>42</sup>. This numerical framework starts from the idea that the class of uniform MPS constitutes a manifold that describes ground states of spin chains, but realizes that the low-energy dynamics around such a ground state is contained within the tangent space on this manifold. In this work, we show that these tangent-space methods can also be applied to the PEPS manifold, and we expect that this will prove extremely useful in the simulation of the low-energy dynamics of two-dimensional quantum matter.

*Acknowledgements*— The authors would like to thank Kai Schmidt and Ruben Verresen for sharing their data. This work is supported by the Research Foundation Flanders, ERC grants QUTE (647905) and ERQUAF (715861), and the EU grant SIQS.

- 
- \* laurens.vanderstraeten@ugent.be
- <sup>1</sup> F. Verstraete, V. Murg, and J. I. Cirac, “Matrix product states, projected entangled pair states, and variational renormalization group methods for quantum spin systems,” *Advances in Physics* **57**, 143–224 (2008).
  - <sup>2</sup> R. Orús, “A practical introduction to tensor networks: Matrix product states and projected entangled pair states,” *Annals of Physics* **349**, 117–158 (2014).
  - <sup>3</sup> U. Schollwöck, “The density-matrix renormalization group in the age of matrix product states,” *Annals of Physics* **326**, 96–192 (2011).
  - <sup>4</sup> J. Haegeman, B. Pirvu, D. J. Weir, J. I. Cirac, T. J. Osborne, H. Verschelde, and F. Verstraete, “Variational matrix product ansatz for dispersion relations,” *Physical Review B* **85**, 100408 (2012).
  - <sup>5</sup> J. Haegeman, S. Michalakakis, B. Nachtergaele, T. J. Osborne, N. Schuch, and F. Verstraete, “Elementary excitations in gapped quantum spin systems,” *Physical Review Letters* **111**, 080401 (2013).
  - <sup>6</sup> V. Zauner-Stauber, L. Vanderstraeten, J. Haegeman, I. P. McCulloch, and F. Verstraete, “Topological nature of spinons and holons: Elementary excitations from matrix product states with conserved symmetries,” *Physical Review B* **97**, 235155 (2018).
  - <sup>7</sup> L. Vanderstraeten, F. Verstraete, and J. Haegeman, “Scattering particles in quantum spin chains,” *Physical Review B* **92**, 125136 (2015).
  - <sup>8</sup> F. Verstraete and J. I. Cirac, “Renormalization algorithms for Quantum-Many Body Systems in two and higher dimensions,” *arXiv* (2004), cond-mat/0407066.
  - <sup>9</sup> D. Poilblanc and N. Schuch, “Simplex  $z_2$  spin liquids on the kagome lattice with projected entangled pair states: Spinon and vison coherence lengths, topological entropy, and gapless edge modes,” *Physical Review B* **87**, 140407 (2013).
  - <sup>10</sup> N. Schuch, J. I. Cirac, and D. Pérez-García, “Peps as ground states: Degeneracy and topology,” *Annals of Physics* **325**, 2153 – 2192 (2010).
  - <sup>11</sup> N. Bultinck, M. Marin, D.J. Williamson, M. B. Şahinoğlu, J. Haegeman, and F. Verstraete, “Anyons and matrix product operator algebras,” *Annals of Physics* **378**, 183 – 233 (2017).
  - <sup>12</sup> J. Haegeman, V. Zauner, N. Schuch, and F. Verstraete, “Shadows of anyons and the entanglement structure of topological phases,” *Nature Communications* **6**, 8284 (2015).
  - <sup>13</sup> M. Iqbal, K. Duivenvoorden, and N. Schuch, “Study of anyon condensation and topological phase transitions from a  $z_4$  topological phase using the projected entangled pair states approach,” *Physical Review B* **97**, 195124 (2018).
  - <sup>14</sup> P. Corboz, A. M. Läuchli, K. Penc, M. Troyer, and F. Mila, “Simultaneous dimerization and  $su(4)$  symmetry breaking of 4-color fermions on the square lattice,” *Physical Review Letters* **107**, 215301 (2011).
  - <sup>15</sup> P. Corboz and F. Mila, “Crystals of bound states in the magnetization plateaus of the shastry-sutherland model,” *Physical Review Letters* **112**, 147203 (2014).
  - <sup>16</sup> P. Corboz, T. M. Rice, and M. Troyer, “Competing states in the  $t$ - $j$  model: Uniform  $d$ -wave state versus stripe state,” *Physical Review Letters* **113**, 046402 (2014).
  - <sup>17</sup> I. Niesen and P. Corboz, “Emergent haldane phase in the  $s = 1$  bilinear-biquadratic heisenberg model on the square lattice,” *Physical Review B* **95**, 180404 (2017).
  - <sup>18</sup> H. J. Liao, Z. Y. Xie, J. Chen, Z. Y. Liu, H. D. Xie, R. Z. Huang, B. Normand, and T. Xiang, “Gapless spin-liquid ground state in the  $s = 1/2$  kagome antiferromagnet,” *Physical Review Letters* **118**, 137202 (2017).
  - <sup>19</sup> D. Poilblanc and M. Mambrini, “Quantum critical phase with infinite projected entangled paired states,” *Physical Review B* **96**, 014414 (2017).
  - <sup>20</sup> J.-Y. Chen, L. Vanderstraeten, S. Capponi, and D. Poilblanc, “Non-abelian chiral spin liquid in a quantum antiferromagnet revealed by an ipeps study,” *arXiv* (2018), 1807.04385.
  - <sup>21</sup> B.-X. Zheng, C.-M. Chung, P. Corboz, G. Ehlers, M.-P. Qin, R. M. Noack, H. Shi, S. R. White, S. Zhang, and G. K.-L. Chan, “Stripe order in the underdoped region of the two-dimensional hubbard model,” *Science* **358**, 1155–1160 (2017).
  - <sup>22</sup> L. Vanderstraeten, M. Mariën, F. Verstraete, and J. Haegeman, “Excitations and the tangent space of projected entangled-pair states,” *Physical Review B* **92**, 201111 (2015).
  - <sup>23</sup> M.T. Fishman, L. Vanderstraeten, V. Zauner-Stauber, J. Haegeman, and F. Verstraete, “Faster methods for contracting infinite 2d tensor networks,” *arXiv* (2017), 1711.05881.
  - <sup>24</sup> P. Corboz, “Variational optimization with infinite projected entangled-pair states,” *Physical Review B* **94**, 035133 (2016).
  - <sup>25</sup> L. Vanderstraeten, J. Haegeman, P. Corboz, and F. Verstraete, “Gradient methods for variational optimization of projected entangled-pair states,” *Physical Review B* **94**, 155123 (2016).
  - <sup>26</sup> M. Rader and A. M. Läuchli, “Finite correlation length scaling in lorentz-invariant gapless ipeps wave functions,” *Physical Review X* **8**, 031030 (2018).
  - <sup>27</sup> P. Corboz, P. Czarnik, G. Kapteijns, and L. Tagliacozzo, “Finite correlation length scaling with infinite projected entangled-pair states,” *Physical Review X* **8**, 031031 (2018).
  - <sup>28</sup> R. P. Feynman, “Atomic Theory of the Two-Fluid Model of Liquid Helium,” *Physical Review* **94**, 262–277 (1954).
  - <sup>29</sup> D. P. Arovas, A. Auerbach, and F. D. M. Haldane, “Extended Heisenberg models of antiferromagnetism: Analogies to the fractional quantum Hall effect,” *Physical Review Letters* **60**, 531–534 (1988).
  - <sup>30</sup> J. Oitmaa, C. Hamer, and W. Zheng, *Series Expansion Methods for Strongly Interacting Lattice Models* (Cambridge University Press, 2006).
  - <sup>31</sup> A. Sen, H. Suwa, and A. W. Sandvik, “Velocity

- of excitations in ordered, disordered, and critical antiferromagnets,” *Physical Review B* **92**, 195145 (2015).
- <sup>32</sup> S. Chakravarty, B. I. Halperin, and D. R. Nelson, “Two-dimensional quantum heisenberg antiferromagnet at low temperatures,” *Physical Review B* **39**, 2344–2371 (1989).
- <sup>33</sup> A. V. Chubukov, S. Sachdev, and J. Ye, “Theory of two-dimensional quantum heisenberg antiferromagnets with a nearly critical ground state,” *Physical Review B* **49**, 11919–11961 (1994).
- <sup>34</sup> A. W. Sandvik and R. R. P. Singh, “High-energy magnon dispersion and multimagnon continuum in the two-dimensional heisenberg antiferromagnet,” *Physical Review Letters* **86**, 528–531 (2001).
- <sup>35</sup> M. Powalski, G. S. Uhrig, and K. P. Schmidt, “Roton minimum as a fingerprint of magnon-higgs scattering in ordered quantum antiferromagnets,” *Physical Review Letters* **115**, 207202 (2015).
- <sup>36</sup> A. Lüscher and A. M. Läuchli, “Exact diagonalization study of the antiferromagnetic spin- $\frac{1}{2}$  heisenberg model on the square lattice in a magnetic field,” *Physical Review B* **79**, 195102 (2009).
- <sup>37</sup> R. R. P. Singh and M. P. Gelfand, “Spin-wave excitation spectra and spectral weights in square lattice antiferromagnets,” *Physical Review B* **52**, R15695–R15698 (1995).
- <sup>38</sup> W. Zheng, J. Oitmaa, and C. J. Hamer, “Series studies of the spin- $\frac{1}{2}$  heisenberg antiferromagnet at  $t = 0$ : Magnon dispersion and structure factors,” *Physical Review B* **71**, 184440 (2005).
- <sup>39</sup> H. Shao, Y. Q. Qin, S. Capponi, S. Chesi, Z. Y. Meng, and A. W. Sandvik, “Nearly deconfined spinon excitations in the square-lattice spin-1/2 heisenberg antiferromagnet,” *Physical Review X* **7**, 041072 (2017).
- <sup>40</sup> M. Powalski, K. P. Schmidt, and G. S. Uhrig, “Mutually attracting spin waves in the square-lattice quantum antiferromagnet,” *SciPost Phys.* **4**, 001 (2018).
- <sup>41</sup> B. Dalla Piazza, M. Mourigal, N. B. Christensen, G. J. Nilsen, P. Tregenna-Piggott, T. G. Perring, M. Enderle, D. F. McMorrow, D. A. Ivanov, and H. M. Rønnow, “Fractional excitations in the square-lattice quantum antiferromagnet,” *Nature Physics* **11**, 62 (2015).
- <sup>42</sup> L. Vanderstraeten, J. Haegeman, and F. Verstraete, “Tangent-space methods for uniform matrix product states,” in preparation.

## APPENDIX: IMPLEMENTING THE PEPS QUASIPARTICLE ANSATZ

In this appendix we provide the details for implementing and optimizing the PEPS excitation ansatz. We work on the square lattice for which the ground state can be represented as a translation- and rotation-invariant PEPS, and we take the case of a translation invariant Hamiltonian with terms acting on a plaquette of four sites. We assume that we have an optimized ground-state approximation, for the details of how to variationally optimize the ground-state PEPS tensor we refer to Ref. 25. In order to make this appendix self-contained, we recapitulate the construction of effective channel environments<sup>22</sup> in a first section, and then explain the excitation ansatz in detail.

### 1. Uniform PEPS and effective environments

We assume that the ground state of the Hamiltonian is given by a PEPS,

$$|\Psi(A)\rangle = \text{Diagram of a 4x4 grid of tensors } A \text{ with wiggly lines on the outer edges.} \quad (1)$$

where the wiggly lines correspond to the physical degrees of freedom. The tensors appearing in the PEPS are all copies of the same tensor  $A$ ,

$$A_{u,r,d,l}^s = \text{Diagram of a single tensor } A \text{ with indices } u, s, r, d, l. \quad (2)$$

and we assume that the tensor is rotation invariant,

$$A_{u,r,d,l}^s = A_{l,u,r,d}^s = A_{d,l,u,r}^s = A_{r,d,l,u}^s, \quad (3)$$

so that the state  $|\Psi(A)\rangle$  is too (everything below can be readily generalized to non-rotation invariant case).

The norm of a PEPS can be represented as

$$\langle \Psi(A) | \Psi(A) \rangle = \text{Diagram of a 4x4 grid of circles with horizontal and vertical lines connecting them, representing the contraction of an } A \text{ tensor with its complex conjugate along the physical dimension, and we have grouped two legs into one in each direction,} \quad (4)$$

where the round tensor represents the contraction of an  $A$  tensor with its complex conjugate along the physical dimension, and we have grouped two legs into one in each direction,

$$\sum_{\substack{\{l, l'\} \\ \{d, d'\}}} \sum_{\substack{\{u, u'\} \\ \{r, r'\}}} \delta_{s, s'} A_{u, r, d, l}^s \bar{A}_{u', r', d', l'}^{s'} \quad (5)$$

The contraction of this infinite tensor network is performed by finding the fixed point of the linear transfer matrix in the form of an MPS on the virtual level. This MPS obeys the fixed-point equation

$$\text{Diagram of a horizontal chain of squares and circles} \propto \text{Diagram of a horizontal chain of squares} \quad (6)$$

Here, the MPS is represented by a triple of tensors  $\{A_l, A_r, C\}$  which obey the conditions

$$\text{Diagram of } A_l \text{ and } C \text{ contraction} = \text{Diagram of } C \text{ and } A_r \text{ contraction}, \quad (7)$$

and

$$\text{Diagram of } A_l \text{ and } A_l \text{ contraction} = (, \quad \text{Diagram of } A_r \text{ and } A_r \text{ contraction} = ). \quad (8)$$

The ‘norm per site’  $f = -\frac{1}{N} \log(\langle \Psi(A) | \Psi(A) \rangle)$  corresponding to the PEPS is then defined as

$$f = -\log \lambda, \quad (9)$$

where  $\lambda$  is given as the leading eigenvalue of the following eigenvalue equations

$$\text{Diagram of } G_l \text{ and } A_l \text{ contraction} = \lambda \text{Diagram of } G_l, \quad \text{Diagram of } A_r \text{ and } G_r \text{ contraction} = \lambda \text{Diagram of } G_r \quad (10)$$

The corresponding eigenvectors  $G_l$  and  $G_r$  are normalized such that

$$\frac{1}{\lambda} \text{Diagram of } G_l \text{ and } G_r \text{ contraction} = \text{Diagram of } G_l \text{ and } G_r \text{ contraction} = 1 \quad (11)$$

We can now rescale the PEPS tensor  $A$  as

$$A \rightarrow A/\sqrt{\lambda}, \quad (12)$$

such that we have  $f = 0$ , and all PEPS expectation values are well-defined in the thermodynamic limit.

In addition, we define a corner tensor  $S$  which is the leading eigenvector of the equation

$$\text{Diagram of a corner tensor contraction} \propto \text{Diagram of a corner tensor } S \quad (13)$$

which can be simplified to

$$\propto \text{Diagram with } S \text{ symbol.} \quad (14)$$

In order to compute expectation values we find four environments  $\{M_l, M_r, C\}_i$  which we use to determine the contraction of the norm of the PEPS as

$$\text{Diagram showing a grid of } M_l, M_r, M_c \text{ tensors and circles.} \quad (15)$$

The MPS tensors  $\{M_l, M_r\}$  are given by  $\{A_l, A_r\}$  but normalized such that the following eigenvalue equation has leading eigenvalue  $\mu = 1$ :

$$\rho = \mu \rho. \quad (16)$$

The PEPS can now be fully normalized by rescaling the corresponding eigenvector  $\rho$  such that

$$\langle \Psi(A) | \Psi(A) \rangle = \rho \text{ --- } C \text{ --- } \rho = 1. \quad (17)$$

We also define the fixed point in the other direction  $\tilde{\rho}$  as

$$\tilde{\rho} = \mu \tilde{\rho} \quad (18)$$

and normalize it such that

$$\rho \text{ --- } \tilde{\rho} = 1. \quad (19)$$

The norm of the PEPS is then also given by

$$\langle \Psi(A) | \Psi(A) \rangle = \rho \text{ --- } M_l, M_r \text{ --- } \tilde{\rho} = 1 \quad (20)$$

We now define the corner environment

$$\text{Diagram showing a corner environment with } M_l, M_r \text{ tensors and } S \text{ symbol.} \quad (21)$$



where the corner matrix  $S$  is normalized such that, again, the norm of the PEPS is one:

$$\langle \Psi(A) | \Psi(A) \rangle = \text{Diagram} = \text{Diagram} = 1. \quad (22)$$

We also define two-site channel fixed points as

$$\text{Diagram} = \mu \text{Diagram}. \quad (23)$$

Because of the redefinition of  $M_l$  and  $M_r$ , the eigenvalue  $\mu$  should be (approximately) one. We also define the other fixed point,

$$\text{Diagram} = \mu \text{Diagram}. \quad (24)$$

Note that we overload the symbols for tensors, where its definition depends on the number of legs it has. The energy density expectation value is given by the two equivalent diagrams

$$e = \text{Diagram} = \text{Diagram}, \quad (25)$$

where we have introduced the dashed lines to indicate the four sites on which the Hamiltonian plaquette operator acts.

## 2. The ansatz wavefunction

We use the following ansatz for an excitation with momentum  $(q_x, q_y)$

$$|\Phi_{\vec{q}}(B)\rangle = \sum_{k,l} e^{iq_x k} e^{iq_y l} \text{Diagram} \quad (26)$$

where the round tensor denotes a new tensor  $B$ ,

$$B_{u,r,d,l}^s = \begin{array}{c} u \quad s \\ \diagup \quad \diagdown \\ \bigcirc \\ \diagdown \quad \diagup \\ d \quad r \end{array}, \quad (27)$$

containing all variational degrees of freedom in the excited state. The overlap between the ground state and an excited state can be easily computed. We first introduce the following notation for a double-layer tensor containing a  $B$  tensor in the ket-level,

$$\begin{array}{c} \{u, u'\} \\ \diagup \quad \diagdown \\ \bigcirc \\ \diagdown \quad \diagup \\ \{d, d'\} \end{array} \begin{array}{c} \{l, l'\} \\ \diagup \quad \diagdown \\ \bigcirc \\ \diagdown \quad \diagup \\ \{r, r'\} \end{array} = \sum_{s, s'} \delta_{s, s'} B_{u, r, d, l}^s \bar{A}_{u', r', d', l'}^{s'}, \quad (28)$$

so that the overlap is given by

$$\langle \Psi(A) | \Phi_{\vec{q}}(B) \rangle = 2\pi\delta(q_x) 2\pi\delta(q_y) \begin{array}{c} \rho \quad \tilde{\rho} \\ \diagup \quad \diagdown \\ \bigcirc \\ \diagdown \quad \diagup \\ \rho \quad \tilde{\rho} \end{array} \begin{array}{c} M_l \\ M_r \end{array} \quad (29)$$

$$= 2\pi\delta(q_x) 2\pi\delta(q_y) \begin{array}{c} \rho \\ \diagup \quad \diagdown \\ \bigcirc \\ \diagdown \quad \diagup \\ \rho \end{array} \begin{array}{c} \rho \\ \diagup \quad \diagdown \\ \bigcirc \\ \diagdown \quad \diagup \\ \rho \end{array} \begin{array}{c} \rho \\ \diagup \quad \diagdown \\ \bigcirc \\ \diagdown \quad \diagup \\ \rho \end{array} \begin{array}{c} \rho \\ \diagup \quad \diagdown \\ \bigcirc \\ \diagdown \quad \diagup \\ \rho \end{array}. \quad (30)$$

The overlap with the ground state can be written as  $\langle \Psi(A) | \Phi_{\vec{q}}(B) \rangle = 4\pi^2 \delta^{(2)}(\vec{q}) \mathbf{g}^\dagger \mathbf{B}$ , so that we confine the variational subspace to tensors that are orthogonal to  $\mathbf{g}$ . Here we have introduced bold-face notation for the vectorized version of a tensor.

As such, the variational subspace is ill defined because of the presence of zero modes. Indeed, the particular choice for the  $B$  tensor

$$\begin{array}{c} \diagup \quad \diagdown \\ \bigcirc \\ \diagdown \quad \diagup \end{array} = e^{iq_x} \begin{array}{c} \diagup \quad \diagdown \\ \square \\ \diagdown \quad \diagup \end{array} \begin{array}{c} \diagup \quad \diagdown \\ \bigcirc \\ \diagdown \quad \diagup \end{array} - \begin{array}{c} \diagup \quad \diagdown \\ \bigcirc \\ \diagdown \quad \diagup \end{array} \begin{array}{c} \diagup \quad \diagdown \\ \square \\ \diagdown \quad \diagup \end{array}, \quad (31)$$

with  $X$  a random matrix, yields a zero state

$$\langle \Phi_{\vec{q}'}(B) | \Phi_{\vec{q}}(B) \rangle = 0. \quad (32)$$

Equivalently, the choice

$$\begin{array}{c} \diagup \quad \diagdown \\ \bigcirc \\ \diagdown \quad \diagup \end{array} = e^{iq_y} \begin{array}{c} \diagup \quad \diagdown \\ \bigcirc \\ \diagdown \quad \diagup \end{array} \begin{array}{c} \diagup \quad \diagdown \\ \square \\ \diagdown \quad \diagup \end{array} - \begin{array}{c} \diagup \quad \diagdown \\ \square \\ \diagdown \quad \diagup \end{array} \begin{array}{c} \diagup \quad \diagdown \\ \bigcirc \\ \diagdown \quad \diagup \end{array}, \quad (33)$$

yields a zero mode.

In general the overlap between two states in our variational space can be written as

$$\langle \Phi_{\vec{q}'}(B') | \Phi_{\vec{q}}(B) \rangle = 2\pi\delta(q_x - q'_x) 2\pi\delta(q_y - q'_y) N_{\vec{q}}(B, B'), \quad (34)$$

and, similarly, for overlaps of the Hamiltonian we find

$$\langle \Phi_{\vec{q}'}(B) | H | \Phi_{\vec{q}}(B) \rangle = 2\pi\delta(q_x - q'_x) 2\pi\delta(q_y - q'_y) M_{\vec{q}}(B, B'). \quad (35)$$

In addition, since the parametrization of the states  $|\Phi(B)\rangle$  is clearly linear in the tensor elements of  $B$ , we can rewrite these expressions as

$$N_{\vec{q}}(B, B') = (\mathbf{B}')^\dagger \mathbf{N}_{\vec{q}} \mathbf{B} \quad (36)$$

$$M_{\vec{q}}(B, B') = (\mathbf{B}')^\dagger \mathbf{M}_{\vec{q}} \mathbf{B}, \quad (37)$$

where  $\mathbf{B}$  denotes the vectorized version of the tensor  $B$ , and  $\mathbf{M}_{\vec{q}}$  and  $\mathbf{N}_{\vec{q}}$  are  $(D^2d)$ -dimensional hermitian matrices.

The variational optimization of the excitation ansatz

$$\min_{B \in \mathcal{R}} \frac{\langle \Phi_{\vec{q}}(B) | H | \Phi_{\vec{q}}(B) \rangle}{\langle \Phi_{\vec{q}}(B) | \Phi_{\vec{q}}(B) \rangle}, \quad (38)$$

can now be rephrased as a generalized eigenvalue problem

$$(\mathbf{P}^\dagger \mathbf{H}_{\vec{q}} \mathbf{P}) \mathbf{x}_{\vec{q}} = \omega(\vec{q}) (\mathbf{P}^\dagger \mathbf{N}_{\vec{q}} \mathbf{P}) \mathbf{x}_{\vec{q}}, \quad (39)$$

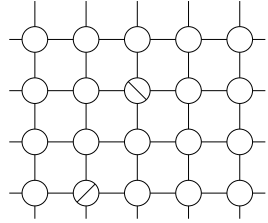
where  $\mathbf{P}$  is a reduced basis for the  $B$  tensors where all zero modes have been eliminated.

### 3. The effective norm matrix

We compute the effective norm matrix, for which we have to compute the matrix elements

$$\langle \Phi_{\vec{q}'}(B') | \Phi_{\vec{q}}(B) \rangle = 2\pi\delta(q_x - q'_x) 2\pi\delta(q_y - q'_y) N_{\vec{q}}(B, B'). \quad (40)$$

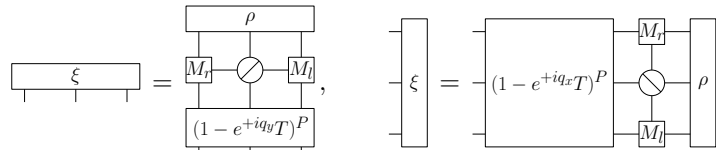
The expression for  $N_{\vec{q}}$  consists of a sum over all relative orientations of  $B$  and  $B'$  tensors, i.e. diagrams of the form

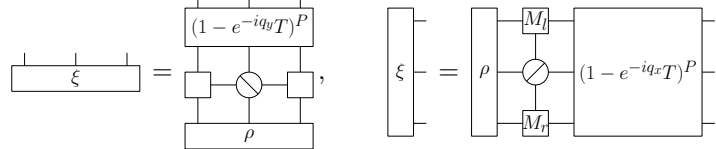

(41)

where we have introduced the tensor notation

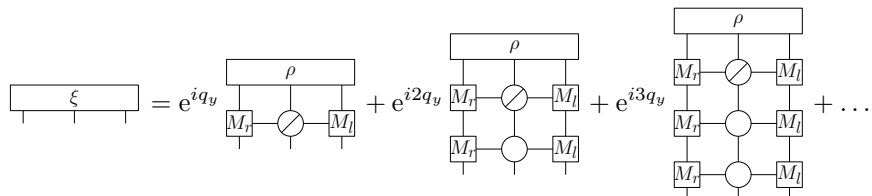
$$\sum_{\substack{\{l, l'\} \\ \{d, d'\}}} \sum_{\substack{\{u, u'\} \\ \{r, r'\}}} \bigcirc = \sum_{s, s'} \delta_{s, s'} A_{u, r, d, l}^s \bar{B}'_{u', r', d', l'}. \quad (42)$$

First we need to define the following tensor capturing the infinite sum of the  $B$  tensor going in the upper channel


(43)


(44)

Here we have introduced the 'pseudo inverse' of a channel operator, which appears whenever we want to take an infinite sum of contributions along a channel. Indeed, if we want to represent


(45)

we should be able to compute

$$\sum_{n=0}^{\infty} e^{iq_y(n+1)} \left( \begin{array}{c} \boxed{M_r} \text{---} \bigcirc \text{---} \boxed{M_l} \\ | \quad | \quad | \end{array} \right)^n. \quad (46)$$

This series converges if the spectral radius of the 'channel operator'  $T$ ,

$$T = \begin{array}{c} \boxed{M_r} \text{---} \bigcirc \text{---} \boxed{M_l} \\ | \quad | \quad | \end{array}, \quad (47)$$

is smaller than one. But, as we have seen above, we have normalized the tensors  $M_l$  and  $M_r$  such that the leading eigenvalue of this operator is exactly one, and the corresponding fixed point is given by  $\rho$ . Therefore we can write

$$\sum_{n=0}^{\infty} e^{iq_y(n+1)} \left( \begin{array}{c} \boxed{M_r} \text{---} \bigcirc \text{---} \boxed{M_l} \\ | \quad | \quad | \end{array} \right)^n = e^{iq_y} \sum_{n=0}^{\infty} e^{iq_y n} \left( \begin{array}{c} \boxed{\rho} \\ \boxed{\bar{\rho}} \\ | \quad | \quad | \end{array} \right) + e^{iq_y} \left( 1 - e^{iq_y} \left( \begin{array}{c} \boxed{M_r} \text{---} \bigcirc \text{---} \boxed{M_l} \\ | \quad | \quad | \end{array} \right) \right)^P, \quad (48)$$

where the notation  $(\dots)^P$  implies that we have projected out the fixed point subspace from the channel operator. The fixed-point projector contains a potential divergence, but, since we always make sure that Eq. (29) is zero, this contribution will always drop out.

These tensors we can use to define the following auxiliary tensor

$$\begin{array}{c} \boxed{\gamma} \\ | \end{array} = e^{-iq_x} \begin{array}{c} \boxed{\rho} \\ | \quad | \quad | \\ \xi \text{---} \bigcirc \text{---} \rho \\ | \quad | \quad | \\ \boxed{(1 - e^{+iq_y T})^P} \end{array} + \begin{array}{c} \boxed{\rho} \\ | \quad | \quad | \\ \rho \text{---} \bigcirc \text{---} \rho \\ | \quad | \quad | \\ \boxed{(1 - e^{+iq_y T})^P} \end{array} \quad (49)$$

and we define three other  $\gamma$  tensors that are related to the one above by a simple rotation and an interchange of the momenta. The full matrix element is then given by

$$\begin{aligned} N_{\vec{q}}(B, B') = & \begin{array}{c} \boxed{\rho} \\ | \quad | \quad | \\ \rho \text{---} \bigotimes \text{---} \rho \\ | \quad | \quad | \\ \boxed{\rho} \end{array} + e^{+iq_y} \begin{array}{c} \boxed{\gamma} \\ | \quad | \quad | \\ \boxed{M_l} \text{---} \bigcirc \text{---} \boxed{M_r} \\ | \quad | \quad | \\ \boxed{\rho} \end{array} \\ & + e^{+iq_x} \begin{array}{c} \boxed{M_l} \\ | \quad | \quad | \\ \rho \text{---} \bigotimes \text{---} \gamma \\ | \quad | \quad | \\ \boxed{M_r} \end{array} + e^{-iq_y} \begin{array}{c} \boxed{\rho} \\ | \quad | \quad | \\ \boxed{M_r} \text{---} \bigotimes \text{---} \boxed{M_l} \\ | \quad | \quad | \\ \boxed{\gamma} \end{array} + e^{-iq_x} \begin{array}{c} \boxed{\gamma} \\ | \quad | \quad | \\ \gamma \text{---} \bigotimes \text{---} \rho \\ | \quad | \quad | \\ \boxed{M_l} \end{array} \end{aligned} \quad (50)$$

$$= \begin{array}{c} \boxed{\rho} \\ | \quad | \quad | \\ \rho \text{---} \bigotimes \text{---} \rho \\ | \quad | \quad | \\ \boxed{\rho} \end{array} + e^{+iq_y} \begin{array}{c} \boxed{\gamma} \\ | \quad | \quad | \\ \boxed{M_l} \text{---} \bigotimes \text{---} \boxed{M_r} \\ | \quad | \quad | \\ \boxed{\rho} \end{array} + \text{rotations.} \quad (51)$$

where three rotated versions of the last diagram should be added with the appropriate momentum factors.



Secondly, we have the sum of disconnected  $h$  operators

$$\eta = \begin{array}{c} \rho \\ \hline \begin{array}{ccccc} & M_r & & & M_l \\ & | & & & | \\ & \bigcirc & & & \bigcirc \\ & | & & & | \\ & M_r & & & M_l \end{array} \\ \hline (1-T)^P \end{array}, \quad (55)$$

We further define the following tensors

$$\xi_l = e^{-iq_x} \begin{array}{c} \rho \\ \hline \begin{array}{ccccc} & \xi & & & M_l \\ & | & & & | \\ & \bigcirc & & & \bigcirc \\ & | & & & | \\ & \xi & & & M_l \end{array} \\ \hline (1 - e^{iq_y} T_l)^P \end{array} + \begin{array}{c} \rho \\ \hline \begin{array}{ccccc} & \rho & & & M_l \\ & | & & & | \\ & \bigcirc & & & \bigcirc \\ & | & & & | \\ & \rho & & & M_l \end{array} \\ \hline (1 - e^{iq_y} T_l)^P \end{array} \quad (56)$$

$$\xi_r = e^{+iq_x} \begin{array}{c} \rho \\ \hline \begin{array}{ccccc} & M_r & & & \xi \\ & | & & & | \\ & \bigcirc & & & \bigcirc \\ & | & & & | \\ & M_r & & & \xi \end{array} \\ \hline (1 - e^{iq_y} T_r)^P \end{array} + \begin{array}{c} \rho \\ \hline \begin{array}{ccccc} & M_r & & & \rho \\ & | & & & | \\ & \bigcirc & & & \bigcirc \\ & | & & & | \\ & M_r & & & \rho \end{array} \\ \hline (1 - e^{iq_y} T_r)^P \end{array} \quad (57)$$

and their two-site versions

$$\begin{aligned} \xi_l &= e^{-2iq_x} \begin{array}{c} \rho \\ \hline \begin{array}{ccccc} & \xi & & & M_l \\ & | & & & | \\ & \bigcirc & & & \bigcirc \\ & | & & & | \\ & \xi & & & M_l \end{array} \\ \hline (1 - e^{iq_y} T_l)^P \end{array} \\ &+ e^{-iq_x} \begin{array}{c} \rho \\ \hline \begin{array}{ccccc} & \rho & & & M_l \\ & | & & & | \\ & \bigcirc & & & \bigcirc \\ & | & & & | \\ & \rho & & & M_l \end{array} \\ \hline (1 - e^{iq_y} T_l)^P \end{array} + \begin{array}{c} \rho \\ \hline \begin{array}{ccccc} & \rho & & & M_l \\ & | & & & | \\ & \bigcirc & & & \bigcirc \\ & | & & & | \\ & \rho & & & M_l \end{array} \\ \hline (1 - e^{iq_y} T_l)^P \end{array} \\ \xi_r &= e^{+2iq_x} \begin{array}{c} \rho \\ \hline \begin{array}{ccccc} & M_r & & & \xi \\ & | & & & | \\ & \bigcirc & & & \bigcirc \\ & | & & & | \\ & M_r & & & \xi \end{array} \\ \hline (1 - e^{iq_y} T_r)^P \end{array} \end{aligned} \quad (58)$$

$$+ e^{+iq_x} \left[ \text{Diagram 1} + \text{Diagram 2} \right]. \quad (59)$$

The Hamiltonian versions of these tensors are

$$\eta_l = \text{Diagram 1} + \text{Diagram 2} \quad (60)$$

$$\eta_r = \text{Diagram 1} + \text{Diagram 2} \quad (61)$$

Here we have introduced the channel operators  $T_l$  and  $T_r$  as

$$T_l = \boxed{M_l} - \bigcirc - \boxed{M_l}, \quad T_r = \boxed{M_r} - \bigcirc - \boxed{M_r}. \quad (62)$$

### *Semi-local contributions*

We can use these tensors to add the contributions where  $B'$  is on either  $B$  or  $h$ , while the other is disconnected. First, we have the contributions where  $h$  is disconnected; we need to sum all diagrams of the form

$$\text{Diagram} \quad (63)$$

where  $h$  is located completely in the upper-left part of the lattice. This sum amounts to the two following diagrams,

$$M_{q_x q_y}^{\text{sl},1}(B, B') = \text{Diagram 1} + \text{Diagram 2} + \text{rotations}, \quad (64)$$

and we have three rotated versions corresponding to the orientations of  $h$  in the other quarters of the lattice.

Secondly, when  $B$  is disconnected, we sum all possible locations of  $B$ , and  $B'$  is located on the first site of  $h$ . All other diagrams are then related through rotations:

$$M_{qxqy}^{\text{sl},2}(B, B') = \left( \begin{array}{c} e^{iq_y} \left( \text{Diagram 1} \right) + e^{iq_x} \left( \text{Diagram 2} \right) \\ + e^{i2q_x} \left( \text{Diagram 3} \right) + e^{-2iq_y} \left( \text{Diagram 4} \right) \\ + e^{-iq_x} \left( \text{Diagram 5} \right) + e^{-iq_y} \left( \text{Diagram 6} \right) \end{array} \right) + \text{rotations.} \quad (65)$$



*Non-local contributions*

We now compute all contributions where we can divide the lattice into two halves, where  $B$  and  $h$  are above the bipartition and the  $B'$  tensor is below the line. That means we will have diagrams of the form

(66)

Do note that we have diagrams which allow for two different bipartitions, for example

(67)

In the following we will only take the diagrams of the left, so that we don't count diagrams twice.

Define the auxiliary tensors

$$\begin{aligned}
 \boxed{\gamma_t} &= e^{+2iq_y} \left( \text{Diagram 1} \right) + e^{iq_y} \left( \text{Diagram 2} \right) \\
 &+ \left( e^{-2iq_x} \left( \text{Diagram 3} \right) + e^{-iq_x} \left( \text{Diagram 4} \right) \right. \\
 &\quad \left. + e^{-2iq_x} \left( \text{Diagram 5} \right) + \left( \text{Diagram 6} \right) \right)
 \end{aligned}$$

$$\begin{aligned}
& + e^{-2iq_x} \left[ \text{Diagram 1} \right] + e^{-iq_x} \left[ \text{Diagram 2} \right] + \left[ \text{Diagram 3} \right] \quad (68)
\end{aligned}$$

and

$$\begin{aligned}
& \left[ \text{Diagram 4} \right] = e^{+2iq_y} \left[ \text{Diagram 5} \right] \\
& + e^{iq_y} \left( \begin{aligned} & e^{-2iq_x} \left[ \text{Diagram 6} \right] + e^{-iq_x} \left[ \text{Diagram 7} \right] \\ & + \left[ \text{Diagram 8} \right] \end{aligned} \right) \quad (69)
\end{aligned}$$

(70)

such that we can define

$$\left[ \text{Diagram 9} \right] = \left[ \text{Diagram 10} \right], \quad \left[ \text{Diagram 11} \right] = \left[ \text{Diagram 12} \right]. \quad (71)$$

Now we are in a position to add all contributions that we can obtain by making a bipartition. We group the terms in four groups, according to the orientation of  $h$ . First we sum the contributions where  $h$  is situated in the up-right corner to  $B'$ , i.e. in the region

$$\left[ \text{Diagram 13} \right], \quad (72)$$

and  $B$  can be anywhere. All terms where  $B$  and  $h$  are to the right of  $B'$  are contained in the  $\gamma$  tensor,

so that we have the following diagrams:

$$\begin{aligned}
 \overline{\alpha_1} &= e^{iq_x} \left( \text{Diagram 1} + e^{iq_x} \text{Diagram 2} \right) \\
 &+ \left( e^{i2q_y} \left( \text{Diagram 3} + \text{Diagram 4} + \text{Diagram 5} \right) \right. \\
 &\left. + e^{-iq_x} \left( e^{iq_y} \left( \text{Diagram 6} + \text{Diagram 7} \right) \right) \right). \tag{73}
 \end{aligned}$$

The diagrams are as follows:

- Diagram 1:** A vertical bar labeled  $\rho$  on the left and  $\gamma$  on the right. A horizontal line with a circle in the middle connects them. Above the circle is a box labeled  $M_l$ . Below the circle is a box labeled  $M_l$ . There are two diamond shapes on the bottom line.
- Diagram 2:** Similar to Diagram 1, but with a different internal structure.
- Diagram 3:** A vertical bar labeled  $\rho$  on the left and  $\eta$  on the right. A horizontal line with a circle in the middle connects them. Above the circle is a box labeled  $\xi$ . Below the circle is a box labeled  $M_l$ . There are two diamond shapes on the bottom line.
- Diagram 4:** Similar to Diagram 3, but with a different internal structure.
- Diagram 5:** A vertical bar labeled  $\rho$  on the left and  $\eta_l$  on the right. A horizontal line with a circle in the middle connects them. Above the circle is a box labeled  $M_l$ . Below the circle is a box labeled  $M_l$ . There are two diamond shapes on the bottom line.
- Diagram 6:** A vertical bar labeled  $\xi_r$  on the left and  $\eta$  on the right. A horizontal line with a circle in the middle connects them. Above the circle is a box labeled  $M_l$ . Below the circle is a box labeled  $M_l$ . There are two diamond shapes on the bottom line.
- Diagram 7:** A vertical bar labeled  $\xi$  on the left and  $\eta_l$  on the right. A horizontal line with a circle in the middle connects them. Above the circle is a box labeled  $M_l$ . Below the circle is a box labeled  $M_l$ . There are two diamond shapes on the bottom line.

Secondly, we have the terms where  $h$  is right above  $B'$  on the right side,

$$\begin{aligned}
 &\text{Diagram 8} \\
 &\tag{74}
 \end{aligned}$$

Diagram 8 is a grid of 6 rows and 4 columns of circles. A dashed rectangle encloses the 4 circles in the 3rd and 4th rows and the 2nd and 3rd columns. A diagonal line connects the top-left circle to the bottom-right circle within this dashed rectangle.

and  $B$  anywhere above  $B'$ , with the diagrams

$$\begin{aligned}
 \overline{\alpha_2} &= e^{2iq_x} \left( \text{Diagram 9} + \text{Diagram 10} \right)
 \end{aligned}$$

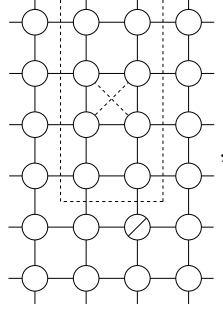
The diagrams are as follows:

- Diagram 9:** A vertical bar labeled  $\rho$  on the left and  $\xi_l$  on the right. A horizontal line with a circle in the middle connects them. Above the circle is a box labeled  $M_l$ . Below the circle is a box labeled  $M_l$ . There are two diamond shapes on the bottom line.
- Diagram 10:** A vertical bar labeled  $\rho$  on the left and  $\xi$  on the right. A horizontal line with a circle in the middle connects them. Above the circle is a box labeled  $\eta$ . Below the circle is a box labeled  $M_l$ . There are two diamond shapes on the bottom line.

$$\begin{aligned}
& + e^{iq_x} \left( e^{i2q_y} \left( \begin{array}{c} \text{Diagram 1} \\ \text{Diagram 2} \end{array} \right) + e^{iq_y} \left( \begin{array}{c} \text{Diagram 3} \\ \text{Diagram 4} \end{array} \right) \right) \\
& + e^{i2q_y} \left( \begin{array}{c} \text{Diagram 5} \\ \text{Diagram 6} \end{array} \right) + e^{iq_y} \left( \begin{array}{c} \text{Diagram 7} \\ \text{Diagram 8} \end{array} \right) \\
& + e^{-iq_x} \left( \begin{array}{c} \text{Diagram 9} \\ \text{Diagram 10} \end{array} \right) + e^{iq_y} \left( \begin{array}{c} \text{Diagram 11} \end{array} \right) .
\end{aligned}
\tag{75}$$

The diagrams are Feynman-like diagrams representing terms in a quantum field theory expansion. They consist of horizontal lines (representing particles) and vertical lines (representing interactions). The diagrams are labeled with various symbols:  $\xi$ ,  $\rho$ ,  $\eta$ ,  $M_l$ ,  $M_r$ ,  $\xi_r$ , and  $\eta$ . The diagrams are arranged in a hierarchical structure, with the first two rows grouped by a large bracket and the last two rows grouped by another large bracket. The diagrams are connected by plus signs, indicating they are summed together. The overall expression is multiplied by  $e^{iq_x}$  and  $e^{-iq_x}$  factors, and the entire expression is enclosed in a large bracket.

Thirdly, we have  $h$  in the region



(76)

with the diagrams

$$\begin{aligned}
 \boxed{\alpha_3} &= \\
 & e^{iq_x} \left( \begin{array}{c} \text{Diagram 1} + \text{Diagram 2} \\ \text{Diagram 3} \end{array} \right) \\
 & + e^{iq_y} \left( \begin{array}{c} \text{Diagram 4} \\ \text{Diagram 5} + \text{Diagram 6} \end{array} \right) \\
 & + e^{i2q_y} \left( \begin{array}{c} \text{Diagram 7} + \text{Diagram 8} \\ \text{Diagram 9} + \text{Diagram 10} \end{array} \right)
 \end{aligned}$$

The diagrams are as follows:

- Diagram 1:** A 3x3 grid with a horizontal bar  $\eta$  at the top. The left and right sides are labeled  $\rho$  and  $\xi$  respectively. Internal nodes are labeled  $M_l$  and  $M_r$ .
- Diagram 2:** A 3x3 grid with a horizontal bar  $\rho$  at the top. The left and right sides are labeled  $\rho$  and  $\xi$  respectively. Internal nodes are labeled  $M_l$  and  $M_r$ .
- Diagram 3:** A 3x3 grid with a horizontal bar  $\xi$  at the top. The left and right sides are labeled  $\rho$  and  $\xi_l$  respectively. Internal nodes are labeled  $M_l$  and  $M_r$ .
- Diagram 4:** A 3x3 grid with a horizontal bar  $\rho$  at the top. The left and right sides are labeled  $\rho$  and  $\xi$  respectively. Internal nodes are labeled  $M_l$  and  $M_r$ .
- Diagram 5:** A 3x3 grid with a horizontal bar  $\rho$  at the top. The left and right sides are labeled  $\rho$  and  $\xi$  respectively. Internal nodes are labeled  $M_l$  and  $M_r$ .
- Diagram 6:** A 3x3 grid with a horizontal bar  $\rho$  at the top. The left and right sides are labeled  $\rho$  and  $\xi$  respectively. Internal nodes are labeled  $M_l$  and  $M_r$ .
- Diagram 7:** A 3x3 grid with a horizontal bar  $\xi$  at the top. The left and right sides are labeled  $\rho$  and  $\xi$  respectively. Internal nodes are labeled  $M_l$  and  $M_r$ .
- Diagram 8:** A 3x3 grid with a horizontal bar  $\rho$  at the top. The left and right sides are labeled  $\rho$  and  $\xi$  respectively. Internal nodes are labeled  $M_l$  and  $M_r$ .
- Diagram 9:** A 3x3 grid with a horizontal bar  $\rho$  at the top. The left and right sides are labeled  $\rho$  and  $\xi$  respectively. Internal nodes are labeled  $M_l$  and  $M_r$ .
- Diagram 10:** A 3x3 grid with a horizontal bar  $\eta$  at the top. The left and right sides are labeled  $\rho$  and  $\xi$  respectively. Internal nodes are labeled  $M_l$  and  $M_r$ .

$$\begin{aligned}
& + e^{-iq_x} \left( e^{i2q_y} \left( \begin{array}{c} \text{Diagram 1: } \xi \text{ box, } \rho \text{ box, } M_r \text{ boxes, } \rho \text{ box} \\ \text{Diagram 2: } \rho \text{ box, } \rho \text{ box, } M_r \text{ boxes, } \rho \text{ box} \end{array} \right) + e^{iq_y} \left( \begin{array}{c} \text{Diagram 3: } \rho \text{ box, } \rho \text{ box, } M_r \text{ boxes, } \rho \text{ box} \\ \text{Diagram 4: } \eta \text{ box, } \rho \text{ box, } M_r \text{ boxes, } \rho \text{ box} \end{array} \right) \right) \\
& + e^{-i2q_x} \left( \begin{array}{c} \text{Diagram 5: } \eta \text{ box, } \xi \text{ box, } M_r \text{ boxes, } \rho \text{ box} \\ \text{Diagram 6: } \xi_r \text{ box, } M_r \text{ boxes, } \rho \text{ box} \end{array} \right). \tag{77}
\end{aligned}$$

The last contribution is given by the orientation of  $h$  as given by

$$\begin{array}{c}
\begin{array}{cccccc}
\circ & \circ & \circ & \circ & \circ & \circ \\
\circ & \circ & \circ & \circ & \circ & \circ \\
\circ & \circ & \circ & \circ & \circ & \circ \\
\circ & \circ & \circ & \circ & \circ & \circ \\
\circ & \circ & \circ & \circ & \circ & \circ \\
\circ & \circ & \circ & \circ & \circ & \circ
\end{array}
, \tag{78}
\end{array}$$

where this time we have to make sure that we don't add the contributions that can be obtained by another bipartition:

$$\begin{array}{c}
\boxed{\alpha_4} \\
\hline
\begin{array}{c} \vdots \\ \vdots \\ \vdots \end{array}
\end{array}
= e^{iq_x} \left( e^{iq_y} \left( \begin{array}{c} \text{Diagram 1: } \eta \text{ box, } M_l \text{ box, } \xi_l \text{ box, } M_r \text{ box} \\ \text{Diagram 2: } \eta_r \text{ box, } M_r \text{ box, } \xi \text{ box} \end{array} \right) \right)$$

$$\left( \begin{array}{c} \text{Diagram 1} \\ e^{2iq_y} \eta \cdot \text{Diagram 2} \\ + e^{iq_y} \eta \cdot \text{Diagram 3} \\ + \eta_r \cdot \text{Diagram 4} \end{array} \right). \quad (79)$$

Now we construct the tensor which adds these four contributions (with  $\alpha_t = \sum_{i=1, \dots, 4} \alpha_i$ )

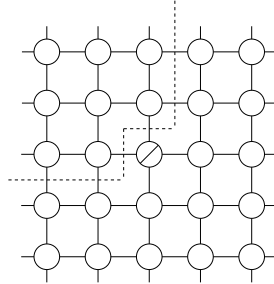
$$\alpha = \begin{array}{c} \alpha_t \\ \hline (1 - e^{iq_y T})^P \end{array}, \quad (80)$$

and, finally

$$M_{\vec{q}}^{\text{nl}}(B, B') = e^{iq_y} \begin{array}{c} \alpha \\ \hline M_l \text{---} \text{---} M_r \\ \hline \rho \end{array} + \text{rotations}. \quad (81)$$

#### Special disconnected contributions

In this subsection, we compute all diagrams which cannot be obtained by making a horizontal bipartition in the lattice where  $B'$  is on the one side, and  $B$  and  $h$  are on the other. We compute all terms for which  $h$  is in the first quarter as defined by  $B'$ , i.e. in the upper-left region



$$, \quad (82)$$

and  $B$  can be anywhere such that there is no bipartition possible. The three other orientations of  $h$  are related through rotations of these diagrams.

All terms are given by

$$\begin{aligned} M_{\vec{q}}^{\text{sp}}(B, B') = & e^{+iq_x} \begin{array}{c} \eta_l \\ \hline M_l \text{---} \text{---} \xi \\ \hline \rho \end{array} + e^{-iq_y} \begin{array}{c} \eta_l \\ \hline M_l \text{---} \text{---} M_l \\ \hline \xi_l \end{array} \\ & + e^{-iq_y} e^{-iq_x} \begin{array}{c} \eta \\ \hline M_l \text{---} \text{---} \text{---} \rho \\ \hline \xi_r \end{array} + e^{-2iq_x} \begin{array}{c} \eta \\ \hline \xi \text{---} \text{---} \text{---} \rho \\ \hline \rho \end{array} \end{aligned}$$

$$\begin{aligned}
& + e^{-iq_y} \left[ \text{Diagram 1} \right] + e^{-iq_x} \left[ \text{Diagram 2} \right] + e^{iq_x} \left[ \text{Diagram 3} \right] + e^{iq_x} e^{iq_y} \left[ \text{Diagram 4} \right] \\
& + e^{iq_y} \left[ \text{Diagram 5} \right] + e^{2iq_y} \left[ \text{Diagram 6} \right] .
\end{aligned} \tag{83}$$

The diagrams are as follows:

- Diagram 1:** A vertical stack of three boxes labeled  $\rho$ ,  $\eta$ , and  $\xi_l$ . The  $\rho$  box is at the top, connected to the  $\eta$  box. The  $\eta$  box is connected to the  $\xi_l$  box. The  $\xi_l$  box is connected to a vertical line that passes through a circle with a diagonal line (representing a measurement or projection). The  $\rho$  box is also connected to a vertical line that passes through a circle with a diagonal line. The  $\eta$  box is connected to a vertical line that passes through a circle with a diagonal line. The  $\xi_l$  box is connected to a vertical line that passes through a circle with a diagonal line.
- Diagram 2:** A vertical stack of three boxes labeled  $\rho$ ,  $\eta$ , and  $\rho$ . The  $\rho$  box is at the top, connected to the  $\eta$  box. The  $\eta$  box is connected to the  $\rho$  box. The  $\rho$  box is connected to a vertical line that passes through a circle with a diagonal line. The  $\eta$  box is connected to a vertical line that passes through a circle with a diagonal line. The  $\rho$  box is connected to a vertical line that passes through a circle with a diagonal line.
- Diagram 3:** A vertical stack of three boxes labeled  $\rho$ ,  $\eta$ , and  $\rho$ . The  $\rho$  box is at the top, connected to the  $\eta$  box. The  $\eta$  box is connected to the  $\rho$  box. The  $\rho$  box is connected to a vertical line that passes through a circle with a diagonal line. The  $\eta$  box is connected to a vertical line that passes through a circle with a diagonal line. The  $\rho$  box is connected to a vertical line that passes through a circle with a diagonal line.
- Diagram 4:** A vertical stack of three boxes labeled  $\rho$ ,  $\eta$ , and  $\rho$ . The  $\rho$  box is at the top, connected to the  $\eta$  box. The  $\eta$  box is connected to the  $\rho$  box. The  $\rho$  box is connected to a vertical line that passes through a circle with a diagonal line. The  $\eta$  box is connected to a vertical line that passes through a circle with a diagonal line. The  $\rho$  box is connected to a vertical line that passes through a circle with a diagonal line.
- Diagram 5:** A vertical stack of three boxes labeled  $\rho$ ,  $\eta$ , and  $\rho$ . The  $\rho$  box is at the top, connected to the  $\eta$  box. The  $\eta$  box is connected to the  $\rho$  box. The  $\rho$  box is connected to a vertical line that passes through a circle with a diagonal line. The  $\eta$  box is connected to a vertical line that passes through a circle with a diagonal line. The  $\rho$  box is connected to a vertical line that passes through a circle with a diagonal line.
- Diagram 6:** A vertical stack of three boxes labeled  $\rho$ ,  $\eta$ , and  $\rho$ . The  $\rho$  box is at the top, connected to the  $\eta$  box. The  $\eta$  box is connected to the  $\rho$  box. The  $\rho$  box is connected to a vertical line that passes through a circle with a diagonal line. The  $\eta$  box is connected to a vertical line that passes through a circle with a diagonal line. The  $\rho$  box is connected to a vertical line that passes through a circle with a diagonal line.